THE SOLAR FLARE SOFT X-RAY DIFFERENTIAL EMISSION MEASURE AND THE NEUPERT EFFECT AT DIFFERENT TEMPERATURES

JAMES. M. McTIERNAN, GEORGE H. FISHER, AND PENG LI
Space Sciences Laboratory, University of California, Berkeley

ABSTRACT

Data from the *Yohkoh* Soft X-ray Telescope (SXT) and Bragg Crystal Spectrometer (BCS) are used to obtain the differential emission measure (DEM) of solar flare soft X-ray plasma. The maximum entropy method is used to obtain the DEM for 80 flares observed by SXT and BCS from 1991 October to 1992 November. We find that it is often difficult to describe the DEM using a monotonically decreasing function; functions with a hump at high temperature are occasionally more useful. From the time history of the DEM, we show that higher temperature plasma peaks earlier and cools faster. We also show that high-temperature plasma (>16.5 MK) is more likely than low-temperature plasma to exhibit the so-called Neupert effect, in which the time derivative of the soft X-ray emission measure is similar to the light curve of the impulsive hard X-ray emission for the flare.

Subject headings: Sun: flares — Sun: X-rays, gamma rays

1. INTRODUCTION

For thermal sources such as the soft X-ray plasma in solar flares, the amount of hot material is given by the emission measure, defined as

$$EM = \int n^2 \, dV \, , \qquad (1)$$

where n is the plasma density and V is the volume of the emitting plasma, for an isothermal source.

From observations, we know that the solar flare soft X-ray plasma is not isothermal. The value of the temperature, T, measured using the isothermal assumption always depends on the energy bandpass of the detector used. This is demonstrated in Figure 1, which shows temperatures measured by the *Yohkoh* Soft X-ray Telescope (SXT) and Bragg Crystal Spectrometer (BCS) for a flare that occurred on 1992 November 5. For all flares, BCS measures a higher value of T than SXT, because the BCS detector sees shorter wavelength, higher energy emission (1.8–5 Å, in four channels) than the SXT detector (3–20 Å, multiple filters); it is more sensitive to high-temperature plasma than SXT (Culhane et al. 1991; Tsuneta et al. 1991). Consequently, when interpreting observations and comparing results with models, it is necessary to know the response of the observing instrument.

For a multitemperature plasma, the differential emission measure (DEM), $q(T)$, is an indication of how much hot material there is as a function of temperature, or

$$EM = \int \frac{d(n^2 V)}{dT} \, dT = \int q(T) \, dT \, , \qquad (2)$$

where EM now represents the emission measure integrated over all temperatures.

The DEM describes the thermal emission from the flare plasma in a way that, in principle, does not depend on the bandpass of a given detector. In this work we will use data from two different detectors, the *Yohkoh* SXT (Tsuneta et al. 1991) and the BCS (Culhane et al. 1991) to obtain the soft X-ray DEM.

The *Yohkoh* SXT has a spatial resolution of $2''.5$ and is sensitive to relatively low temperature (3–20 MK) plasma. The SXT observes flares with five different broadband filters, which gives it the ability to estimate the plasma temperature and emission measure using filter ratios (McTiernan et al. 1993). As shown by Tsuneta et al. (1991), it is difficult to use the SXT alone in deriving the DEM distribution because of the extremely broad, overlapping temperature responses for the different filters.

The *Yohkoh* BCS observes flares in four channels, observing lines of S XV (5.01–5.11 Å), Ca XIX (3.16–3.19 Å), Fe XXV (1.83–1.89 Å), and Fe XXVI (1.76–1.80 Å). These are designed to obtain temperature and emission measure in the range from 10 to 50 MK. With the combination of the SXT and BCS, we can cover the range from 3 to 50 MK.

Our use of BCS differs from previous uses; past studies of BCS data have concentrated on obtaining diagnostics using the good spectral resolution of BCS in the individual channels. Here the BCS is treated as a broadband detector; the line photon flux in each BCS channel is summed and those data are treated in the same way as the SXT data. All information about the plasma motion is lost, since motion affects the line shape and position within the channel, but we gain the ability to estimate the DEM, which until now has not been done using *Yohkoh* data. (Note that the emission from moving plasma is still included in the calculation; mass motion does not affect the total number of photons emitted in the line.) The SXT data are summed over their own spatial resolution (the SXT images used are partial frame 64 × 64 flare-mode images), since BCS is a full-Sun instrument.

There has never been a study of the DEM distribution for a large sample of solar flares. Some work has been done regarding the solar flare DEM in the past, from work with Solrad and Skylab data (Dere & Cook 1979), through the *Solar Maximum Mission (SMM)* era (Sylwester, Schrijver, & Mewe 1980; Jakimiec et al. 1984; Gabriel et al. 1984; Strong et al. 1986), but these studies covered only a small sample of events. Recent DEM determinations have been done mostly using EUV (*EUVE*) and X-ray (*ASCA*) observations of quiet stars and stellar flares, with very little solar work done (Del Zanna et al. 1996; Monsignori-Fossi et al. 1996; Mewe et al. 1996, 1997; Cully et al. 1997).

Other calculations have used *Yohkoh* BCS data to find the velocity differential emission measure, which gives the
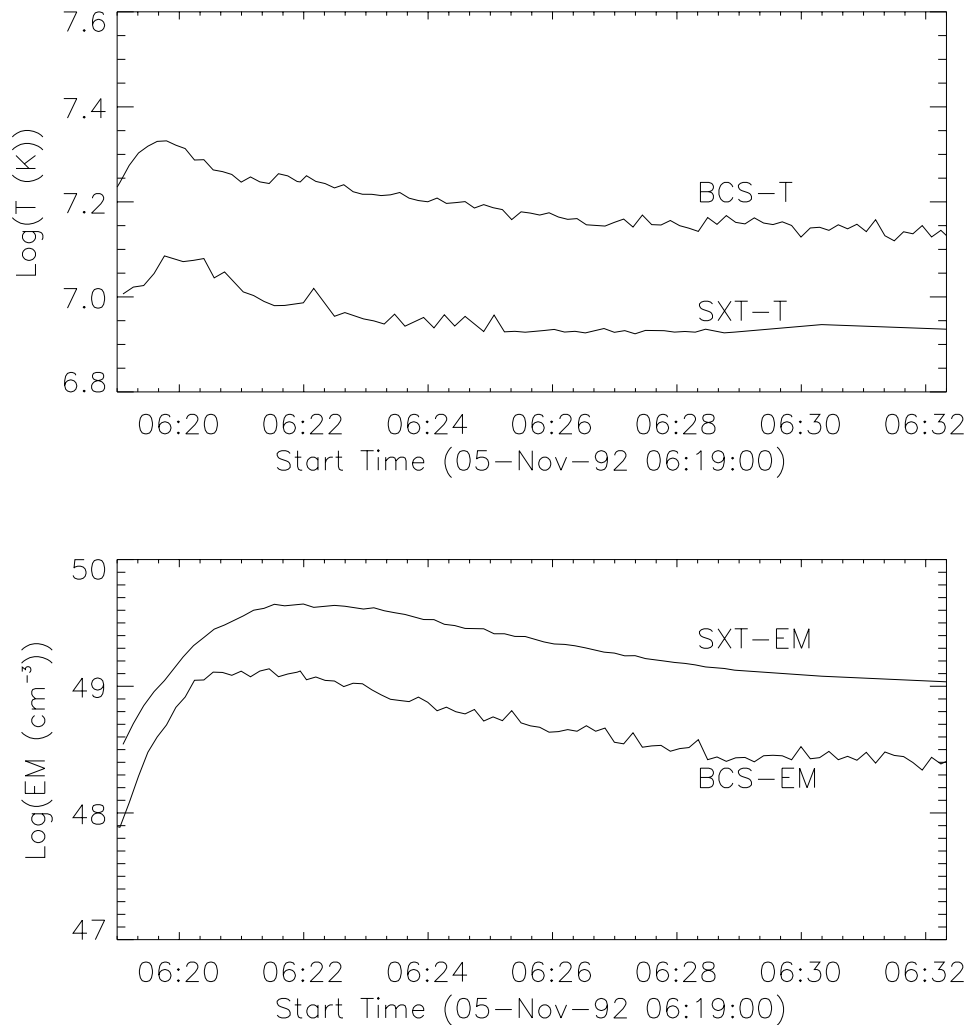
FIG. 1.—*Yohkoh* SXT and BCS temperature and emission measure vs. time for the 1992 November 5 flare

amount of flare plasma as a function of fluid velocity, but not as a function of temperature (Newton, Emslie, & Mariska 1995, 1996). We make no determination of velocity, so the work described here should be considered complementary to that of Newton et al.

We have a number of objectives for this study. The DEM is one of the few observationally inferred quantities that can be directly compared with theoretical models. Flare heating models, which predict temperature, pressure, and density as functions of space and time, also predict the DEM. For different flare heating mechanisms, the models may produce different results. There have been many hydrodynamic models of flares, e.g., Antiochos & Sturrock (1976, 1978); Antiochos & Krall (1979); Nagai & Emslie (1984); Emslie (1985); Fisher, Canfield, & McClymont (1985a, 1985b, 1985c); Mariska, Emslie, & Li (1989); Serio et al. (1991); Jakimiec et al. (1992); Emslie, Li, & Mariska (1992); and Li, Emslie, & Mariska (1993). Since there are few recent DEM reconstructions derived from observations, authors rarely show their theoretical DEM. In the above list of references, only Emslie (1985) and Mariska et al. (1989) actually include plots of the DEM as a function of temperature. To compare with observations, it is necessary to reduce the model DEM down to single-temperature results (Sylwester et al. 1993; Antonucci & Martin 1995; Reale et al. 1997).

We also would like to examine the so-called Neupert effect as it applies to the behavior of plasma at different temperatures. It is well known that the soft X-ray time derivative is similar to the hard X-ray (or microwave) light curve (Neupert 1968; Dennis & Zarro 1993). This is known as the "Neupert effect." It has been shown in theoretical work (e.g., Li et al. 1993) that this effect can be reproduced if the flare energy release occurs in the form of nonthermal electrons. The nonthermal electrons lose their energy via Coulomb collisions in the lower corona and upper part of the chromosphere. The temperature rises, and a high-pressure region forms that drives material both upward and downward (chromospheric evaporation and chromospheric condensation). The coronal temperature and density are enhanced as the evaporated material rises, resulting in increased soft X-ray emission.

In this case the hard X-ray light curves are proportional to the time profile of the accelerated electrons. The soft X-ray emission, which is emitted from the plasma heated by the nonthermal electrons, is proportional to the accumulated energy deposited by the electrons up to a given time, even when losses due to thermal conduction and mass motion are considered. The soft X-ray emission is thus proportional to the time integral of the profile of the input electrons, and we therefore expect the Neupert effect

between soft and hard X-rays. Note that the small impulsive soft X-ray loop footpoint sources that have been observed in some SXT flares are not accounted for by this model (Hudson et al. 1994; McTiernan et al. 1993; Li, McTiernan, & Emslie 1997).

If we know how the DEM behaves with respect to the hard X-ray electrons, we can place constraints on flare models, whether they involve chromospheric evaporation by hard X-ray (HXR) electrons or other heating mechanisms. In particular, we can show how the plasma exhibits the Neupert effect and whether this effect takes place in the high-temperature plasma, the low-temperature plasma, or in all of the plasma.

We can also use the DEM to study the behavior of the plasma after the HXR burst, to see if there is an extended period of heating beyond that expected from the hard X-ray light curve. The DEM gives us a much better tool for studying the evolution of the soft X-ray plasma energy than does the isothermal approximation (although it is still limited, as discussed later). If energy in the soft X-ray plasma continues to increase beyond the end of the hard X-ray burst, then additional heating is needed.

2. DATA ANALYSIS

For these calculations we use data from the Al.1 (1400 Å thick aluminum), Al12 (12 μm thick aluminum), and Be119 (119 μm thick beryllium) filters of SXT and the Ca XIX and Fe XXV channels of BCS. All of the line flux in the Ca XIX channel is included in the fit, including any due to moving plasma. Bulk motion can cause the line profile to be blueshifted or redshifted, but this has no effect on our analysis unless the shifts are large enough to drive the photon flux out of the channel, a situation that does not occur for any of the flares in our sample. A sample BCS Ca XIX channel spectrum is shown in the top panel of Figure 2.

The middle and bottom panels show sample spectra for the Fe XXV channel, where the situation is more difficult; in many cases the line profile can be shifted enough so that photons in the complex of lines on the right are not detected; this is shown in the middle panel. In other cases the line profile is shifted to the left, in which case there may be extra photons. This is shown in the bottom panel. These shifts in the Fe XXV channel are due not to plasma motion, but instead to the design of the instrument; the wavelength
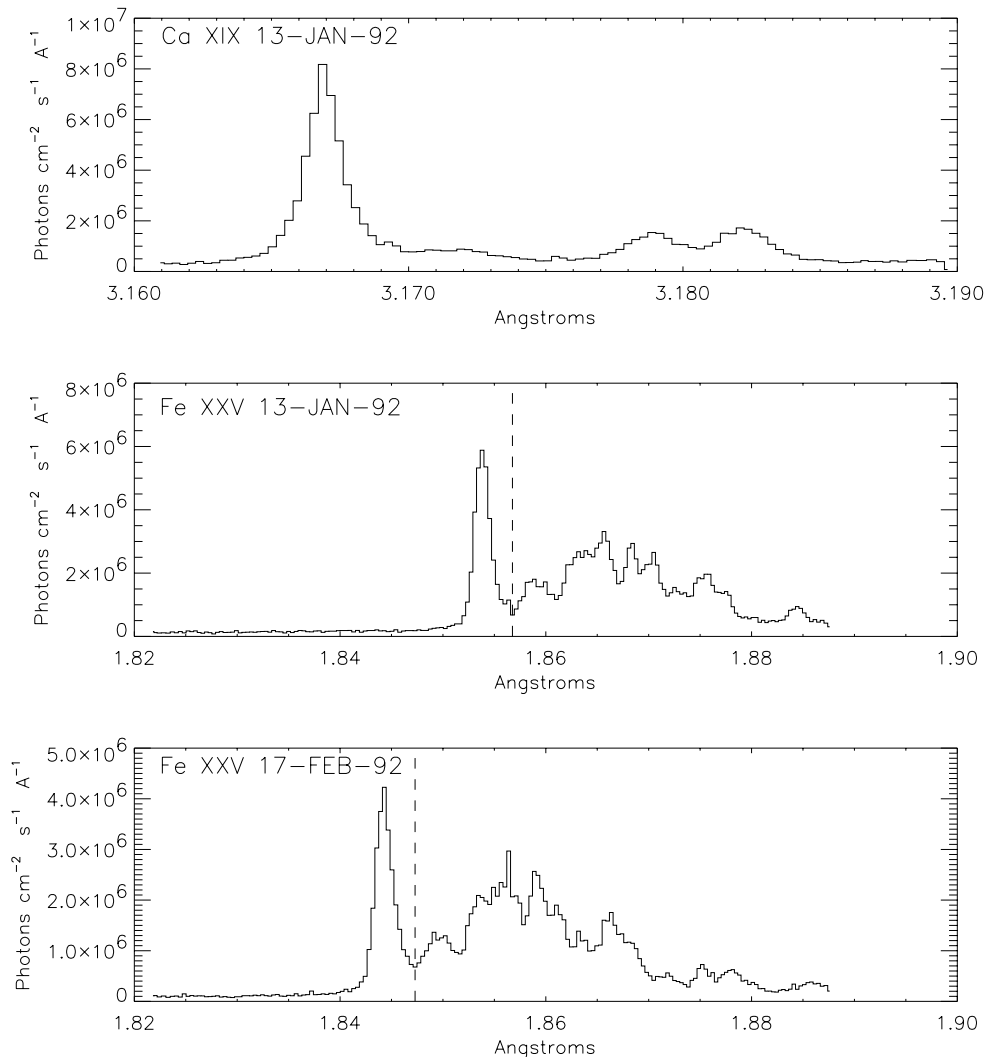

FIG. 2.—BCS spectra: The spectrum in the Ca XIX channel at the peak of Ca XIX emission for a flare of 1992 January 13 (*top panel*). The Fe XXV channel spectrum at the peak of Fe XXV emission for the 1992 January 13 flare (*middle panel*). The Fe XXV channel spectrum at the peak of Fe XXV emission for a flare of 1992 February 17 (*bottom panel*). The nominal wavelength of the Fe XXV resonance line is 1.508 Å. Only the data to the left of the dashed line in the Fe XXV channel are used in our study.
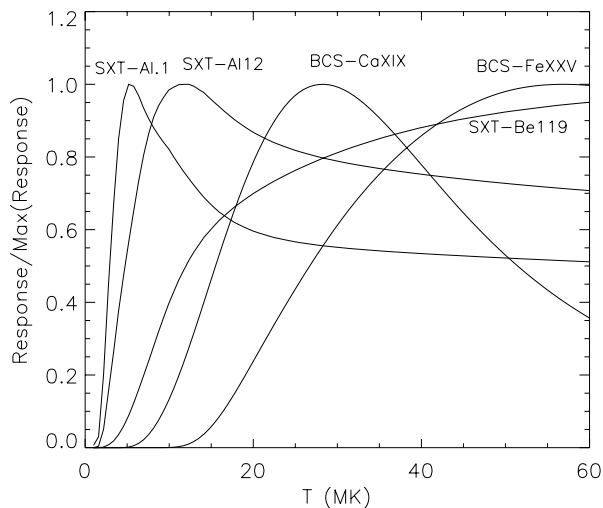
FIG. 3.—Normalized T response for the SXT filters and BCS channels used. Note that the SXT responses extend to high temperatures. Since the T responses are so broad, we do not expect to resolve features in the DEM smaller than a few MK.

of a line that is actually observed by BCS has some dependence on the position of the flare, since it depends on the angle of the incident photons relative to the BCS crystal (Bragg angle; see Culhane et al. 1991). This also happens for the Ca XIX channel, but the effect on the total line flux is negligible, since there is no line emission near the channel edges.

To avoid the problems caused by the line complex on the right of the Fe XXV range, we only use the part of the channel that includes the Fe XXV resonance line, i.e., the part of the spectrum to the left of the vertical line in the plots. Note that this vertical line is chosen for a given flare by averaging the minimum point between the resonance line and the line complex for all of the spectra of the flare. This quantity is constant during flares; for the 1992 January 13 flare the observed wavelength at the minimum is $1.857 \pm 0.003 \, \text{\AA}$.

A plot of the temperature responses for the different channels/filters is shown in Figure 3. The BCS responses are obtained using the IDL program BCS_SPEC, which is distributed as part of the *Yohkoh* software package. The solar coronal abundances used in the *Yohkoh* SXT and BCS software are adopted from Meyer (1985).

3. TEST DATA

To model the DEM, we divide the temperature range into four bins and assign an emission measure to each bin. The amount of emission measure in the bins is then varied to minimize χ^2. We use four bins since we have five data points; the minimization routine used, AMOEBA (Press et al. 1986), is not stable unless there are fewer bins than data points.

This histogram-DEM fits the data well, often resulting in reduced χ^2-values, which approach unity; for example, the average reduced χ^2-value for histogram-DEM fits for the 1992 November 5 flare shown in Figure 1 is 2.5. We improve the solution by using the histogram-DEM as the starting point for a maximum entropy method (MEM) calculation. (The MEM algorithm is the same as that used for *Yohkoh* HXT images; see Sakao 1994.) The MEM calcu-

lation does not converge unless its starting point is very close to the final answer; thus, the good starting point given by the histogram-DEM is absolutely necessary. (For a review of DEM calculations using different methods, including MEM, see Fludra & Sylwester 1986.)

Note that the units of the DEM in this paper are EM/ $(10^{47} \, \text{cm}^{-3} \, \text{MK})$, so that the total emission measure is the integral of the DEM over T, not $\ln(T)$.

Some sample test calculations are shown in Figure 4. For the test calculations, an initial DEM is assumed and integrated over the temperature responses. This is used as input to a Monte Carlo calculation in which a large number of data sets is generated from the original by randomly varying each data point by an amount of up to 2%. (This value was chosen because typical uncertainties in the actual data are of order 2%.) We then obtain a DEM from each data set, and average the results to obtain the final DEM. The uncertainty for the final DEM at each temperature is given by its standard deviation. The top panel of Figure 4 shows the results for a DEM that is a decreasing power law in temperature, a model DEM with which we have had some success in previous work (McTiernan 1996). The solid curve shows the initial DEM, the dashed line shows the histogram-DEM, and the solid histogram with error bars shows the final DEM, which is very close to the initial test DEM. Note that the deviations between the initial and final DEM are the largest at the lowest temperatures (2–4 MK). This is because there is very little temperature response in any of the filter or channel bandpasses at low T. Thus, the lowest T DEM can vary by a large amount and still have only a small effect on the observed data.
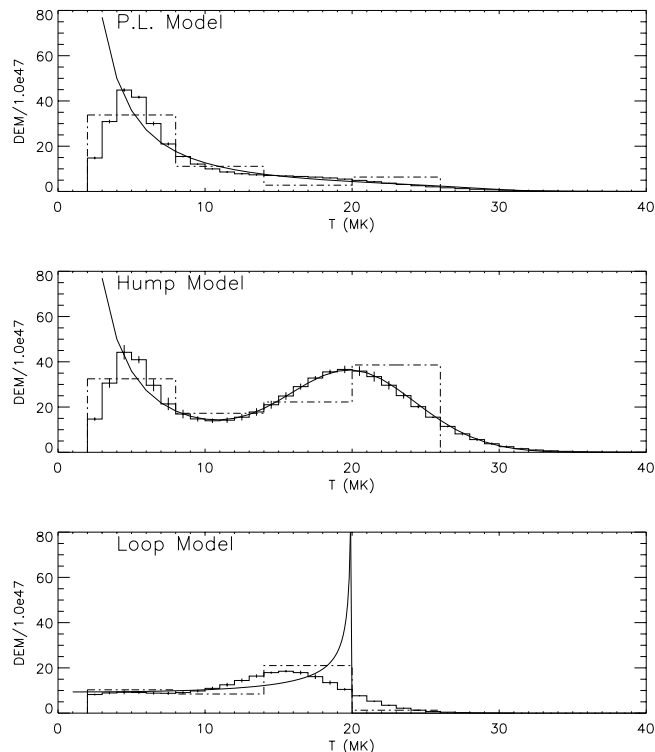

FIG. 4.—Model DEM tests: The top panel shows a DEM that is a decreasing power law in T. The solid curve is the input model DEM. The dot-dashed line is a histogram fit to the model in 4 bins. The histogram with error bars is the MEM fit to the data. In the middle panel, the model DEM is a power law plus a broad hump centered at 20 MK. In the bottom panel, a static loop model is used.

In the middle panel of Figure 4 we test the model using a two-component DEM, in this case a power-law T dependence with a broad hump with a peak at 20 MK. Again, the test results fit the original distribution well.

In the bottom panel, we test the model using a DEM obtained from loop model calculations of Fisher & Hawley (1990). The model is for a "static" loop, in which the heating and cooling of the flaring loop takes place slowly enough so that loop scaling laws are obeyed at all times. Fisher & Hawley studied flare loops in three limiting cases, "strong evaporation," "static," and "strongly condensing." For each case the DEM has a sharp cusp at the loop apex temperature, which is also the maximum temperature. For the evaporation case, the DEM varies as $T^{-1/2}$ below the cusp; for the static loop the DEM is constant below the cusp and the condensing loop model has a DEM that is proportional to T below the cusp.

The loop model shown in the bottom panel of Figure 4 has the high-temperature cusp, but the calculation does not return the cusp shape, instead returning a broad hump. The peak of the hump in the "observed" DEM is 3 MK below the original cusp, with some emission measure existing at temperatures above the original peak. This is due to the lack of good temperature resolution; there is no good way to distinguish temperature structures of less than a few MK. It is not due to the assumed uncertainties. To try to reproduce the cusp, the calculation was done with no random variation of the data in each filter/channel. The resulting DEM still has a broad hump. This DEM solution has a reduced χ^2-value of 0.0003, and each data point is within 0.01% of the initial value. Beyond this point, the MEM solution oscillates; the cusp cannot be reproduced.

4. RESULTS

The DEM inversion analysis described above was carried out for 92 flares that occurred between 1991 October and 1992 November. For a number of flares, no model fitted the data particularly well; in some cases it is obvious that there is a source seen by BCS that is not present in the SXT data. This happens when SXT is observing a flare at one location and another flare occurs at a different position. In flare mode, SXT does not shift its observing region to observe the new flare; thus, SXT does not see all of the emission that BCS does, since BCS observes the entire Sun. In other cases, there are different data gaps for the two different instruments that are too large for interpolation. For the rest of the flares that did not fit well, the flux in the Fe xxv channel was always seriously underestimated by the model; for these cases, either there was a high-temperature component that was missed or the Fe xxv response is incorrect. This could be due to abundance variations or ionization nonequilibrium effects—if the Fe xxv ion is overabundant, there will be more counts in the channel. We will return to these events on an individual basis in the future.

Note that by "a good fit" we mean a reduced χ^2-value of less than or close to unity. In practice, a "good fit" means that the photon fluxes in each channel/filter are within 1% or 2% of the observed data for the entire flare. The uncertainties in the SXT data are a combination of photon-counting statistics, subtraction of the CCD dark current, scattering by the neutral density filter used to increase the SXT dynamic range, and data compression/uncompression. It turns out that the uncertainty due to Poisson statistics for the large number of photons involved in the SXT filters (which can be as high as 10^6 or 10^7 per filter) are small and are often smaller than the uncertainties due to the other sources. This is different from the situation for spatially resolved SXT images, for which Poisson uncertainties dominate (McTiernan et al. 1993). The total SXT uncertainties are typically of order 1%; for example, for the flare shown in Figure 1 of 1992 November 5 the uncertainty in the Be119 filter data ranges from 0.9% to 1.7%.

The uncertainties for BCS channels are relatively larger than those for SXT, typically ranging from 1% to 5%. This includes the Poisson uncertainties in the line photon flux and the continuum flux. The continuum flux is subtracted from the total photon flux in each channel to obtain the total line photon flux. (The number of photons per BCS data point typically ranges from 10^2 to a few times 10^4 per channel). A 1% systematic uncertainty is added to the data for both SXT and BCS to account for the possibility of unknown factors, such as calibration or abundance uncertainties.

The uncertainties are propagated through the entire calculation. The uncertainties for the MEM-DEM are calculated using a routine developed for *Yohkoh* HXT images by Metcalf et al. (1996). In calculations for which there is no standard error propagation formula (e.g., the calculation of peak times for curves and derivatives), the Monte Carlo method, as described in the discussion of the test data, was used.

The final sample contains 80 flares; DEM distributions were derived with 9 s time resolution, for ~ 30 to ~ 100 points for each flare.

As might be expected, results for real flares do not look like model results. The DEM for flares of 1992 January 13 and 1992 February 19 is shown in Figures 5 and 6. In each figure, the DEM is shown at four different times. In each plot the dash-dotted line is the histogram-DEM, in four temperature bins, and the solid line is the MEM-DEM. For each flare, the four plots correspond to (1) the first available BCS data interval (the accumulation time for the intervals is 9 s), (2) a point during the rise phase, (3) the BCS-Fe xxv channel maximum, (4) the SXT-Al.1 maximum.

Our loop models typically have a DEM that increases with T, as we have discussed, and the flares have DEMs that decrease with T. The exception to this is the strong evaporation model, for which there is a $T^{-1/2}$ dependence at low temperatures but also a cusp at the apex temperature. If the loop models are correct, we would expect to see a hump near the maximum temperature and a relatively low, flat DEM for low temperatures, as in the bottom panel of Figure 4. This would be true even in the case of strong evaporation for which the DEM decreases by only a factor of 2 between 5 and 15 MK. Instead we see a large low-T component with either a long high-T tail or a relatively small high-T hump. If we fit a power law to the decreasing part of the low-temperature component for the DEMs shown in Figures 5 and 6, we find that the power-law index ranges from -1.0 to -2.5, much larger than the -0.5 expected in the strong evaporation limit.

There is another way to show that the loop models do not agree with the data. We can simply take the loop model DEM, integrate over the temperature responses, and compare with the observed count rates in SXT and BCS. For example, the loop model used in the bottom panel of Figure 4 results in a ratio of Ca xix counts to Al.1 counts of 0.0015. In our sample of 80 flares, this ratio reaches a value
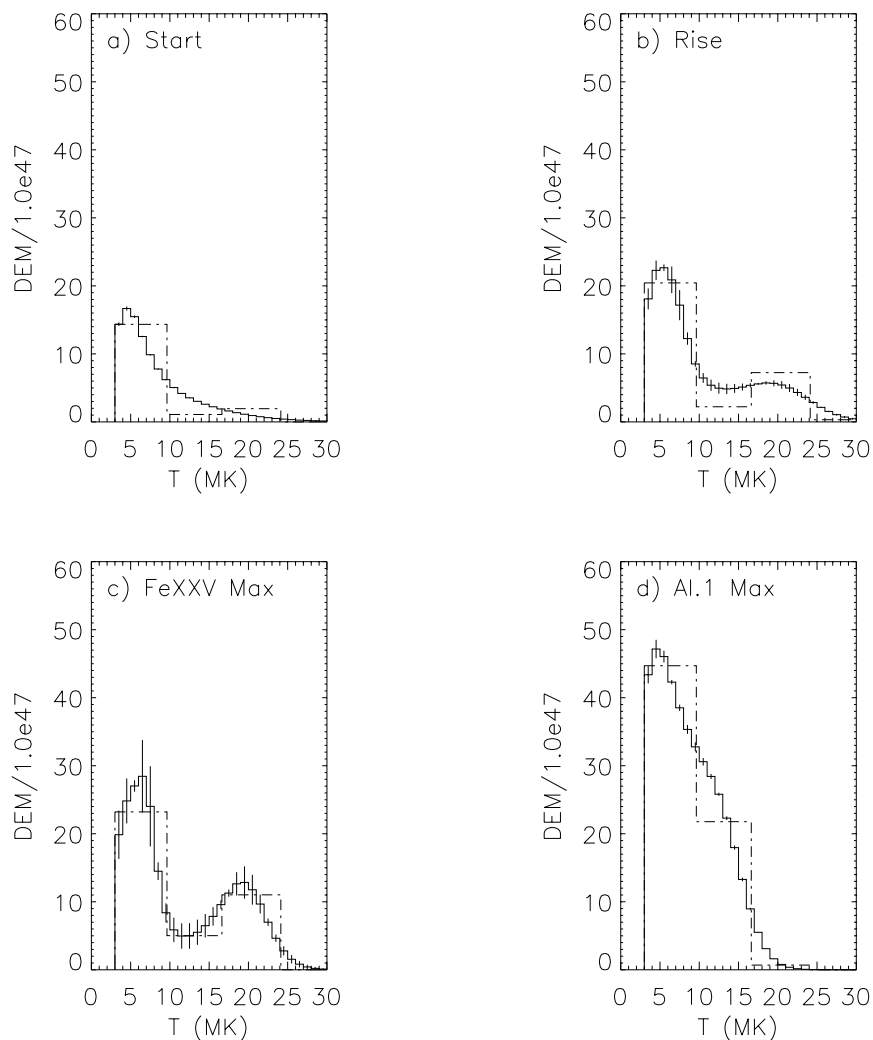
FIG. 5.—DEM for four different times for the flare of 1992 January 13. The dash-dotted line is the histogram-DEM, in four bins (in some cases only three may be visible; the fourth bin has too little emission measure to be seen), and the solid line is the MEM-DEM.

that high once, for 72 s of a flare that occurred on 1991 December 18. For most flares, the Ca XIX/Al.1 ratio is a factor of 3 smaller (0.0005 ± 0.0002). If the cusp is moved to a lower temperature, 13 MK, to account for the low Ca XIX/Al.1 ratio, then there is no response in the Fe XXV resonance line; the resulting Fe XXV/Al.1 counts ratio is 2.0×10^{-5}. This low a value for the Fe XXV/Al.1 ratio is seen for five of the 80 flares in the sample, at the very end of each flare, so a low-temperature cusp is possible, but only at the very end of a few flares.

Note that the models of Emslie (1985) and Mariska et al. (1989), which return differential emission measures that increase with temperature, are also not consistent with these data.

4.1. Two Components

For the 1992 January 13 flare (Masuda et al. 1994) there is a distinct high-temperature hump in the DEM. Nine of the 80 flares in the sample show high-temperature humps with peak values that are at least twice the height of the minimum DEM between the hump and the low-T component. Typically, the minimum between the two components is reached in the 10–15 MK range and the peak

of the hump is in the range 18–27 MK. There is no correlation between this behavior and flare size or position (see Table 1). The January 13 flare is unique in that it has the largest hump, with a peak high-T DEM that reaches $\frac{1}{3}$ of the value of the low-T DEM.

Note that the hump is necessary for these cases. We have attempted to fit the results with monotonically decreasing functions (single and broken power-law fits, with high-T cutoffs), and these do not fit the data. For example, in the time range for which the hump is prominent for the 1992 January 13 flare, the best monotonically decreasing power-law and broken power-law fits to the data have reduced χ^2-values between 4 and 8, while for the histogram and MEM DEM, for the entire flare, $\chi^2 \lesssim 1$. Both the histogram DEM and the broken power-law fits are four parameter fits, with five data points, and therefore 1 dof. The probability of occurrence for the histogram DEM fits is $\gtrsim 0.3$ and that for the broken power-law fits ranges from 0.005 to 0.05 during the time when the hump is noticeable.

Note that early in the flare, and at the end of the flare, when the hump is not there, the power law, broken power law, histogram and MEM all give $\chi^2 \lesssim 1$, so the power-law fits are certainly acceptable at those times. The advantage of
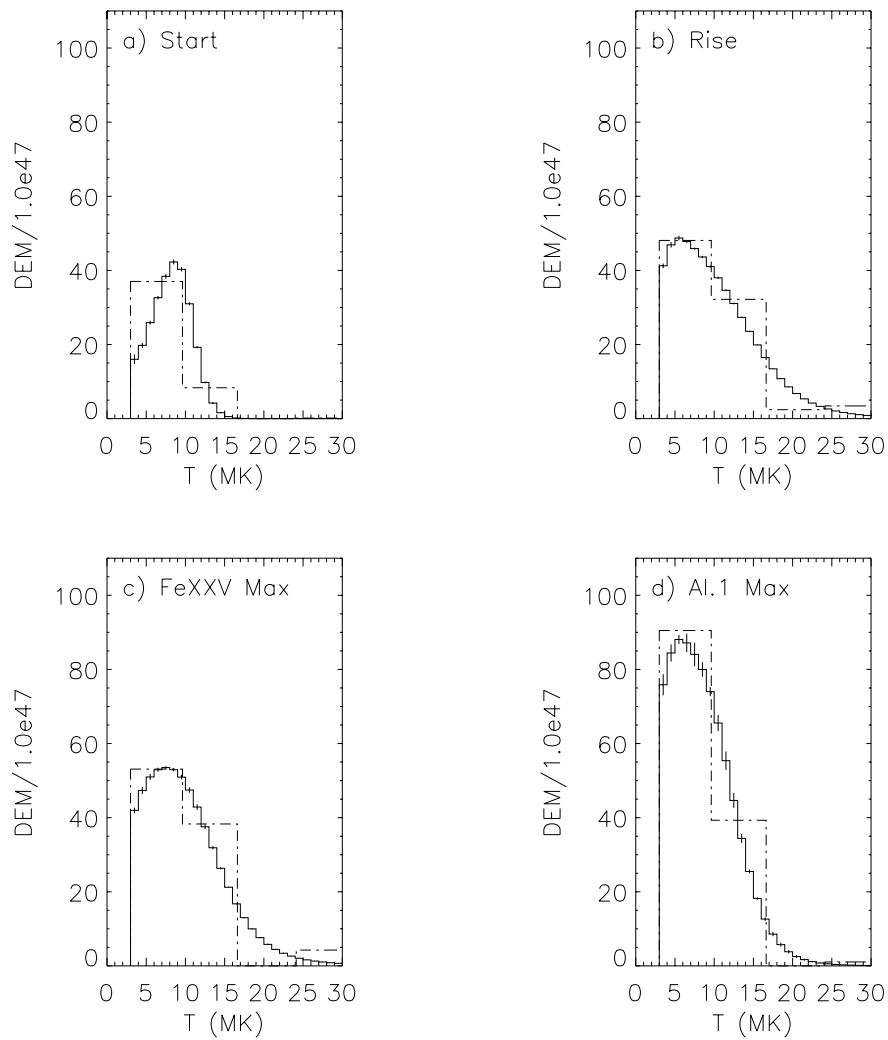
Fig. 6.—DEM for four different times for the flare of 1992 February 19. The format is the same as in Fig. 5.

using the MEM DEM is that it can exhibit the behavior of both the monotonically decreasing DEM and the hump DEM.

When the high-temperature hump is present, the results look very much like results obtained from *SMM* data for a flare of 1980 April 8 by Strong et al. (1986). The high-T component appears during the rise phase, then increases in emission measure, while decreasing in temperature, until it merges with the low-T component. The behavior is qualitatively similar for the cases that do not show a distinct high-T hump. The high-T DEM is an extended tail on the low-T DEM. This tail is more prominent early in the flare and it eventually merges with the low-T component as the flare cools.

4.2. *Thermal Energy, High versus Low Temperatures*

The high-T DEM can account for a substantial amount of energy, even though it is small relative to the DEM at low T. If we assume that the pressure, P, inside the emitting volume, V, is uniform (Strong et al. 1986), then the total thermal energy $(3/2)PV$ is

$$E_{\rm th} = 3kV^{1/2}\left[\int_0^\infty T^2 q(T)\,dT\right]^{1/2}. \qquad (3)$$

For the sake of comparison, we divide the energy range into two regimes, separated by a critical temperature, $T_c = 16.5$ MK, so that "high-T" plasma has $T \geq T_c$ and "low-T" plasma has $T < T_c$. If we assume that, in addition to spatially uniform pressure, the total volume of the soft X-ray flare plasma does not change with time, we find

$$E_{\rm lo} = 3kV^{1/2}\left[\int_0^\infty T^2 q(T)\,dT\right]^{-1/2}\int_0^{T_c} T^2 q(T)\,dT \qquad (4)$$

for the thermal energy of the low-T plasma and

$$E_{\rm hi} = 3kV^{1/2}\left[\int_0^\infty T^2 q(T)\,dT\right]^{-1/2}\int_{T_c}^\infty T^2 q(T)\,dT \qquad (5)$$

for the thermal energy of the high-T plasma. These quantities are plotted for the 1992 January 13 flare in the top panel of Figure 7, for the energy in the low- and high-temperature ranges and the total energy.

Since the rest of this paper will often refer to comparisons between the "low-" and "high-" temperature ranges, the seemingly arbitrary choice of 16.5 MK as the dividing line between these ranges should be justified. This value was chosen after an inspection of the data showed that the time of the peak value of the high-T thermal energy and the times of peaks of the derivative of the high-T energy are

TABLE 1

Flare Characteristics

Date, Time (UT)	GOES	Position (deg)	Time Lag (s)	α	Two Components?	Neupert Effect High T	Low T	Total
1991 Oct 24, 06:29:00	M1.2	S9E62	140	0.18	No	Yes	No	Yes
1991 Oct 26, 00:13:41	M1.1	S16E34	160	0.12	No	...	...	...
1991 Oct 28, 01:08:58	M1.1	S13E3	476	0.09	No	...	...	...
1991 Oct 29, 09:59:33	M1.2	S14W15	144	...	No	No	No	No
1991 Oct 31, 09:11:02	M1.0	S14W39	136	0.15	No	Yes	No	Yes
1991 Nov 9, 03:16:37	M1.5	N20E19	274	0.11	No	No	No	No
1991 Nov 17, 05:10:59	C7.7	N20W80	72	...	No	...	...	...
1991 Nov 17, 18:33:31	M1.9	S13E82	59	0.20	No	Yes	No	Yes
1991 Dec 8, 16:03:11	M1.4	N16E12	78	...	No	...	...	...
1991 Dec 10, 04:02:28	C9.3	S15E90	93	0.26	No	...	...	...
1991 Dec 12, 17:06:17	M1.3	S17W29	37	0.70	No	...	...	...
1991 Dec 15, 14:23:33	M1.0	N5W41	120	0.05	Yes	...	...	...
1991 Dec 16, 03:13:58	C7.8	S12E70	73	0.29	No	Yes	No	No
1991 Dec 16, 06:39:37	M1.6	S12E67	102	0.70	No	Yes	No	Yes
1991 Dec 16, 22:06:12	C7.4	S12E59	56	0.17	No	...	...	...
1991 Dec 18, 10:27:52	M3.5	S14E90	298	0.14	Yes	...	...	...
1991 Dec 26, 21:41:00	M4.2	S16E19	315	0.72	No	Yes	No	No
1992 Jan 5, 13:21:11	M1.9	S12E8	198	...	No	Yes	No	No
1992 Jan 7, 04:09:29	M1.5	S15W10	401	1.35	Yes	No	No	No
1992 Jan 7, 20:24:11	C8.9	S15W20	123	0.11	No	No	No	No
1992 Jan 13, 17:29:56	M2.0	S16W90	436	0.17	Yes	Yes	No	Yes
1992 Jan 30, 02:30:28	M1.6	S2W1	191	0.55	No	Yes	No	Yes
1992 Jan 30, 13:57:13	M1.8	S14W46	125	0.32	No	Yes	No	Yes
1992 Feb 3, 06:59:52	M1.2	S11E29	98	0.21	No	...	...	...
1992 Feb 6, 00:19:37	C9.9	N13E84	71	0.99	No	...	...	...
1992 Feb 7, 11:56:26	M3.7	S18W51	163	0.79	No	Yes	Yes	Yes
1992 Feb 9, 03:02:31	M1.2	S17W76	273	0.41	No	...	...	...
1992 Feb 17, 15:42:39	M1.9	N15W79	229	0.58	No	Yes	No	No
1992 Feb 19, 03:52:22	M3.7	N4E84	232	0.20	No	No	No	No
1992 Feb 19, 23:28:23	C7.7	N1E66	73	0.36	No	...	...	...
1992 Feb 26, 01:38:14	M1.3	S15W90	95	0.17	No	Yes	No	Yes
1992 Feb 29, 20:42:20	M1.7	S12W26	518	0.65	No	...	...	...
1992 Mar 25, 18:48:17	C7.4	N5E45	122	...	No	...	...	...
1992 Apr 24, 12:51:49	M1.4	N10E4	295	...	No	...	...	...
1992 Apr 24, 19:19:02	M1.2	N13W1	27	0.40	No	Yes	Yes	Yes
1992 Jun 7, 01:45:07	M2.7	N7E10	168	0.32	No	Yes	No	Yes
1992 Jun 8, 08:47:14	M1.5	N7W7	122	0.23	No	...	...	...
1992 Jun 23, 10:59:38	C3.6	N10W39	331	0.47	No	Yes	No	No
1992 Jun 23, 23:22:38	C3.4	N11W45	158	0.23	No	...	...	...
1992 Jun 24, 09:39:48	C2.2	N11W51	41	...	No	...	...	...
1992 Jun 24, 18:53:52	C3.6	N10W57	40	0.20	No	...	...	...
1992 Jun 24, 23:55:07	C3.7	N10W58	151	0.06	No	...	...	...
1992 Jun 25, 18:03:46	M1.4	N10W72	826	0.27	Yes	Yes	No	Yes
1992 Jul 3, 09:52:37	M2.1	N12E28	70	...	Yes	Yes	No	No
1992 Jul 4, 22:49:24	C6.9	S13E89	121	0.18	No	...	...	...
1992 Jul 5, 19:58:49	M1.1	S13E86	60	0.01	No	...	...	...
1992 Jul 11, 15:22:57	C5.3	S14E3	388	0.57	No	...	...	...
1992 Jul 12, 17:21:57	C4.2	N16W87	83	0.10	No	...	...	...
1992 Jul 13, 08:04:42	C7.6	S9W4	117	0.30	No	...	...	...
1992 Jul 14, 17:49:10	C6.0	S11W32	108	0.20	No	No	No	No
1992 Jul 15, 02:00:54	C4.2	S11W36	122	0.15	No	Yes	No	No
1992 Jul 15, 03:50:13	C5.3	S23W17	119	0.31	No	...	...	...
1992 Jul 16, 01:11:39	C5.0	S12W43	144	0.19	No	...	...	...
1992 Jul 17, 21:10:53	C7.1	S9W64	94	0.28	No	Yes	No	No
1992 Jul 17, 22:38:45	C5.3	S11W87	165	0.18	No	...	...	...
1992 Jul 18, 01:35:48	C5.1	S14W89	155	0.26	No	...	...	...
1992 Jul 18, 05:09:45	C5.8	S14W89	99	0.40	No	...	...	...
1992 Jul 30, 22:34:27	NA	N19E33	85	0.47	No	...	...	...
1992 Aug 11, 13:49:06	C7.2	S14W43	184	0.15	Yes	Yes	No	No
1992 Aug 16, 13:56:10	C2.9	N16E26	103	0.24	No	...	...	...
1992 Aug 17, 23:59:52	C4.3	N19E1	9	...	No	No	No	No
1992 Aug 18, 13:27:37	C1.8	N18W7	45	...	No	...	...	...
1992 Aug 24, 01:13:13	C2.2	N15W90	76	0.07	No	...	...	...

TABLE 1—*Continued*

Date, Time (UT)	GOES	Position (deg)	Time Lag (s)	α	Two Components?	Neupert Effect		
						High T	Low T	Total
1992 Aug 24, 06:09:31......	C2.5	N16W86	159	...	No	...	...	...
1992 Sep 4, 01:37:53........	NA	S9W7	30	...	No	...	...	...
1992 Sep 7, 08:57:10........	M1.2	S11W55	257	0.05	Yes	No	No	No
1992 Sep 10, 22:54:30	M3.2	N14E44	185	0.34	No	Yes	No	Yes
1992 Sep 11, 06:08:38	M1.4	N15E34	64	0.27	No	No	No	No
1992 Sep 15, 01:59:20	C2.6	N14W79	41	...	No	...	...	...
1992 Sep 16, 23:51:07	C3.7	N14W40	174	0.12	No	...	...	...
1992 Sep 30, 04:52:00	C2.9	N6E25	62	...	No	...	...	...
1992 Oct 5, 09:27:21........	M2.0	S8W89	250	0.37	Yes	Yes	No	No
1992 Oct 7, 10:11:10........	M1.3	S7E30	119	1.30	No	...	...	...
1992 Oct 12, 21:52:12	C2.5	S16W88	72	0.05	No	...	...	...
1992 Oct 22, 18:44:18	C5.1	S8E13	0	...	No	...	...	...
1992 Oct 22, 20:31:16	C3.2	N3W17	107	0.19	No	...	...	...
1992 Oct 23, 22:50:33	C6.6	N2W34	44	0.50	No	...	...	...
1992 Oct 26, 00:52:38	C5.5	S14E56	106	0.18	No	...	...	...
1992 Oct 27, 22:19:27	C5.4	N7W90	68	0.33	No	...	...	...
1992 Nov 5, 06:20:22	M2.0	S18W89	138	0.08	No	Yes	Yes	Yes

close to the same times for the counts in the Fe xxv resonance line. (This is true for all of the flares, not only the 1992 January 13 flare.) In Figure 3, the response of the Fe xxv line is at 10% of its peak value at 16.5 MK. Thus, when we refer to "high-T" plasma, we are referring to the plasma that causes most of the response in the Fe xxv line. All of the rest is "low-T" plasma. It should be noted that we
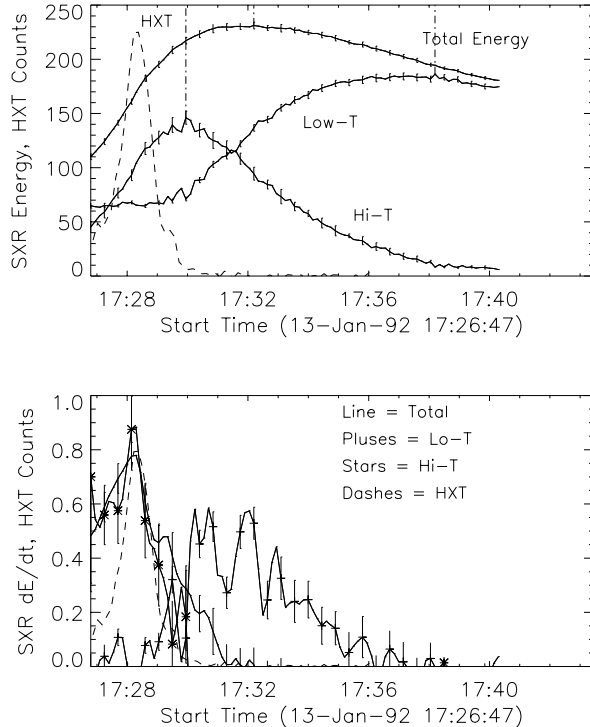

FIG. 7.—Thermal energy as a function of time for the 1992 January 13 flare (*top panel*). The curves for total energy, low-T (<16.5 MK) energy, and high T are so annotated. The HXT time profile is indicated by the dashed line. The derivatives of the energy curves, along with the normalized HXT count rate for hard X-rays above 33 keV (*bottom panel*). The solid line represents the total energy, the line with plus signs represents low-T energy, and the line with stars represents the high-T energy. Error bars are shown for every third point, 27 s apart.

obtain nearly the same results for our comparisons using a value for T_c anywhere in the range 15–20 MK.

As can be seen from Figure 7, the high-T thermal energy peaks earlier and cools faster. An original motivation for this study was to see how the plasma cooling time varies as a function of T. For the 1992 January 13 flare the e-folding energy loss time is 330 s for the high-T plasma. The BCS flare-mode observations did not last long enough for us to get a reasonable cooling time for the low-T component (this is true for most of the flares in the study). Instead, since there is very little high-T plasma left late in the flare, we assume that all of the plasma seen by SXT is low temperature and we use SXT Al.1/Al12 observations to obtain the energy loss time. In this way we find a cooling time of 1890 s for the low-T component. If we define α as the ratio of high-T to low-T cooling times, we find α = 0.17.

If a plasma cools by heat conduction, then the cooling time for a plasma decreases with increasing temperature; the conductive cooling time is $\tau_c \propto T^{-5/2}$. If the plasma cools by radiation, then the cooling time increases with increasing T; $\tau_r \propto T^{3/2}$. (This expression for τ_r is valid if the slope of the radiative loss function for high T is −0.5; Cargill, Mariska, & Antiochos 1995.) Our results are not directly comparable to these cooling times, since the cooling times are calculated by assuming an isothermal plasma with a temperature that varies with time and we calculate the decay time of the energy in the plasma in different temperature ranges. The plasma in the interval $q(T)dT$ at one time is not necessarily the same as the plasma in the same interval at a later time.

We can, nevertheless, guess that the fact that the cooling time decreases with increasing T indicates that conduction plays a role in the cooling of the thermal plasma. Whether conduction dominates at all temperatures is not clear. Models that have the appropriate DEM distributions need to be found, and the cooling times must be calculated from those models for comparisons.

4.3. *The Neupert Effect for High and Low Temperatures*

The bottom panel of Figure 7 shows a comparison of the time derivatives of the low-T, high-T, and total plasma

energy with the count rate in the 33–93 keV range and hard X-rays as seen by the *Yohkoh* HXT. The data are smoothed over 27 s time resolution to smooth fluctuations in the data before the derivative is calculated. The high-T derivative peaks at the same time as the hard X-rays and drops to zero when the hard X-rays drop to the background level. This is a clear example of the Neupert effect.

The low-T derivative is not similar to the HXT curve at all. It remains positive for 7 minutes after the HXT burst. The increase in low-T plasma energy after the HXT burst looks as if it is due to cooling of the high-T plasma; the low-T component is relatively constant up until the end of the HXT burst and then increases as the high-T component decreases. Note that the low-T plasma energy is greater than the high-T plasma energy at the start of the flare, thus all of the energy does not initially go into the high-T plasma.

The total energy derivative peaks at the same time as the hard X-rays, but it remains positive until 2 minutes after the HXT burst. The peak in the total energy time profile is broad, and in fact the maximum energy could occur anywhere from 1 to 3 minutes after the burst. The energy increase after the HXT emission is gone indicates that there may be another heating source besides nonthermal electrons, but given the uncertainty in the total energy peak position, we cannot say this for sure.

Once the DEM behavior is understood, it is easy to explain the time variations seen in the SXT and BCS data. The top plot of Figure 8 shows the data from the Al.1 (*line*) and Be119 (*line with plus signs*) filters of SXT and the Fe xxv

channel of BCS (*stars*) for the same flare. The bottom plot shows the time derivatives of the same data, along with the HXT data. For this case, the curves have been arbitrarily scaled. The Fe xxv channel is mostly sensitive to high-T plasma, and its derivative closely matches the hard X-ray time profile. The Be119 filter is sensitive to both low- and high-T plasma; its derivative has a peak with the HXT burst and remains positive long after the HXT burst. The Al.1 filter is sensitive to high- and low-T plasma but is much more sensitive to low-T plasma than the Be119 filter. Its derivative has a peak with the HXT burst but also has a peak long after the HXT burst. The Al.1 brightness increases (i.e., has a positive derivative) until 17:37 UT. The late increase in Al.1 counts is not due to extra heating, however; the total energy decreases after 17:32 UT. Instead, it is due to cooling of the high-T plasma and the corresponding increase in low-T plasma. The plasma moves into the temperature range where the Al.1 filter is more sensitive and the Al.1 brightness increases, even though the total energy in the plasma is decreasing.

Our point is that a knowledge of the DEM is necessary before one can interpret the Neupert effect and determine whether there is extended heating beyond that due to non-thermal electrons. If, for example, only SXT data are included, then it is easily shown that heating lasts for a long time after the HXT burst and that the Neupert effect is not necessarily present. If only BCS data are included then the Neupert effect is obvious and heating ends with the hard X-ray burst. In reality, the answer may be somewhere in between.

The 1992 January 13 flare is typical in the way it shows the Neupert effect, but all flares do not necessarily behave in the same way. Figure 9 has the same format as Figure 7, for a flare occurring on 1992 February 19. Here the soft X-ray derivatives do not look like the HXT time profile, and they all remain positive after the HXT emission returns to the background level. The derivative of the high-T component and the total energy have peaks just before and 1 minute after the HXT peak. The second peak occurs after the end of the HXT burst. The low-T component derivative has a small peak at the point where the HXT burst peaks and a higher peak later in the flare, long after the HXT burst. The behavior of the low- and high-T components relative to each other is similar to the 1992 January 13 flare, but their relation to the HXT time profile is different.

Consistency or nonconsistency with the Neupert effect was determined by an automated procedure that correlates positive soft X-ray derivatives with HXR emission above the background level. For each flare, in each temperature range, a Neupert "score" is calculated as follows: for each time interval, the soft X-ray and hard X-ray light curves are compared. For a given interval, if the soft X-ray time derivative and the hard X-ray count rate have the same sign (i.e., if both are positive, or if both are negative or zero) then one is added to the score. If the signs of the soft X-ray time derivative and the hard X-ray counts are opposite, then one is subtracted. The score is then divided by the total number of time intervals. Flares with scores that are close to 1.0 (in a possible range from -1.0 to 1.0) can be considered to be consistent with the Neupert effect. Flares with low scores are not consistent with the Neupert effect.

For example, the Neupert scores for the 1992 January 13 flare are 0.95 ± 0.03, -0.02 ± 0.09, and 0.75 ± 0.08, for the high-T energy, low-T energy, and the total energy, respec-
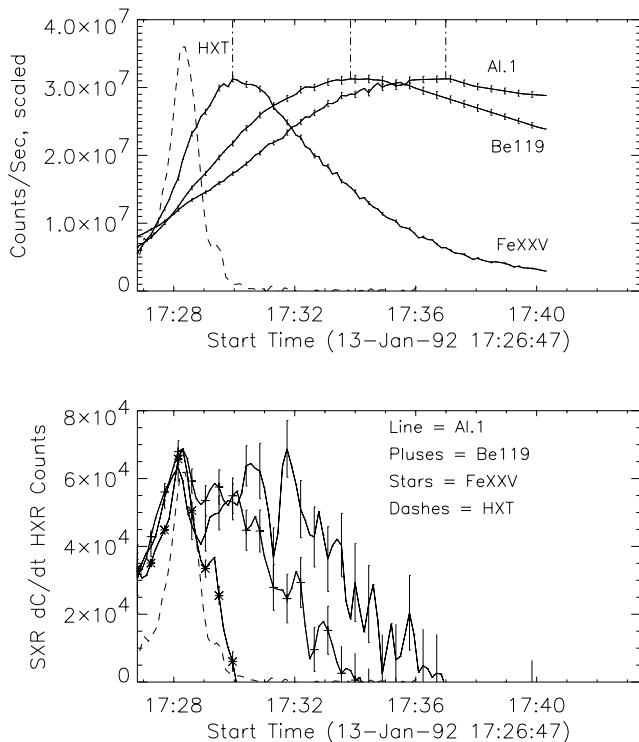

FIG. 8.—SXT and BCS data for the 1992 January 13 flare (*top panel*). The curves for SXT Al.1 data, SXT Be119 data, and BCS Fe xxv data are so annotated. The HXT time profile is indicated by the dashed line. The derivatives of the count rates, along with the normalized HXT count rate for hard X-rays above 33 keV (*bottom panel*). The solid line represents SXT Al.1 data, the line with plus signs represents SXT Be119 data, and the line with stars represents BCS Fe xxv data.
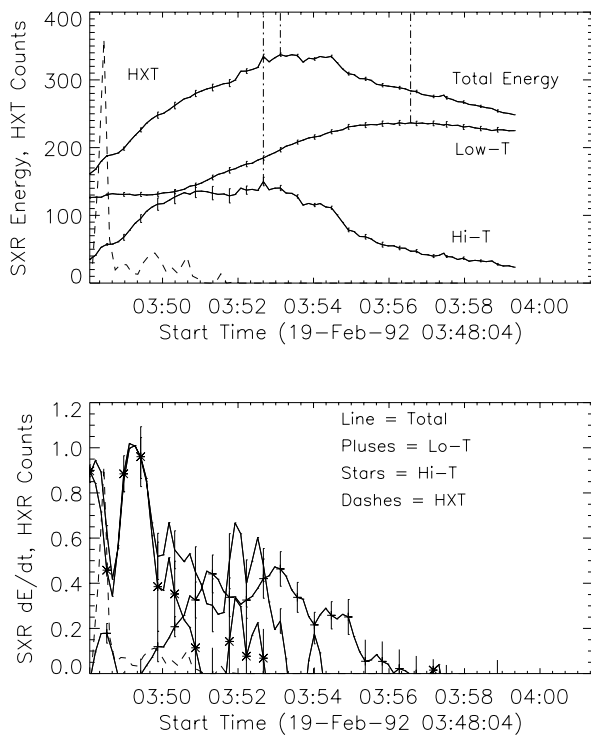
FIG. 9.—Thermal energy as a function of time for the 1992 February 19 flare (*top panel*). The curves for total energy, low-T (<16.5 MK) energy, and high T are so annotated. The HXT time profile is indicated by the dashed line. The derivatives of the energy curves, along with the normalized HXT count rate for hard X-rays above 33 keV (*bottom panel*). The solid line represents the total energy, the line with plus signs represents low-T energy, and the line with stars represents the high-T energy. Error bars are shown for every third point, 27 s apart.

tively. The high-T plasma energy and total energy are consistent with the Neupert effect, as can be seen from Figure 7. The scores for the 1992 February 19 flare are 0.30 ± 0.07, -0.38 ± 0.07, and 0.16 ± 0.03. The uncertainties for each flare were calculated using a Monte Carlo method in which the SXR energy and HXR count rate were varied randomly, by an amount up to their uncertainties. This was done for a large number of trial data sets; the final score for a given flare is the average of the scores for the trial data sets, and the uncertainty in the score is the standard deviation of the set of trial scores.

5. THE FULL SAMPLE

Results for the entire sample of 80 flares are shown in Table 1. For each flare, the table shows the date, the peak time of the Fe xxv emission, the *GOES* X-ray class, the flare position on the disk from SXT, the time lag between the peak of the high-T energy and the peak of the low-T energy (i.e., the low-T peak time minus the high-T peak time), α (the ratio of the high-T decay time to the low-T decay time), whether or not there is a high-temperature hump in the DEM at any point for the flare and whether or not the emission is consistent with the Neupert effect in the high-T range, the low-T range, and for the total energy.

From the table we find that the low-T peak occurs after the high-T peak for all but one flare. For 63 of the 65 flares for which we were able to calculate decay times for both the low-T and high-T components, the ratio α is less than 1. It is clear that the high-temperature plasma (>16.5 MK) peaks earlier and decays faster than the low-temperature plasma. This is a characteristic of conductive cooling, as

mentioned previously, but a combination of conductive and radiative cooling cannot be ruled out.

Only nine of the flares had a high-temperature hump in the DEM. These humps are always smaller than the low-T DEM. (Here we have defined a "hump" as follows: the DEM decreases to a minimum, then increases with increasing T to a peak value that is more than twice the size of the above-mentioned minimum.) This does not rule out the possibility of plasmas with two separate components for the rest of the flares, it simply means that any separate high-T component is not large enough for us to resolve with our limited temperature resolution. There is no correlation between the presence of high-T humps and flare size or position, but we should note that most of the flares in this sample are in a limited size range, from high C class to low M class. We could not analyze larger flares because BCS saturates for large flares. Large flares may indeed have relatively larger high-T components, since the average temperature for flares increases with flare size (Feldman et al. 1996). There is no way for us to make that determination.

There are 33 flares in the sample that have a peak HXT background-subtracted count rate of greater than 100 counts s^{-1} in the energy range above 33 keV and no large data gaps, for which we can make the Neupert effect comparison. At high temperature, these flares neatly divide into two groups; there are 24 flares that have Neupert scores of greater than 0.60 and can be said to be consistent with the Neupert effect and nine flares that have scores of less than 0.42 and are not consistent. There are no borderline cases. To test whether 24 of 33 flares is a significant correlation, we do the same comparison, except in this case each soft X-ray light curve is compared with a random hard X-ray curve drawn from the same sample. This is repeated a number of times in yet another Monte Carlo calculation. From the random sample, for high-T emission, we would expect 15 (± 2) flares to have a score greater than 0.60, so the number of flares that shows consistency with the Neupert effect in the original sample is greater than what would arise from random chance. For low-temperature radiation, only three of the 33 flares are consistent with the Neupert effect; 5 (± 2) would be expected from a random sample. For total plasma energy, 14 of the 33 flares are consistent with the Neupert effect; 10 (± 2) would be expected from a random sample.

We conclude that the Neupert effect is a high-T phenomenon. High-temperature plasma, such as that observed by the *Yohkoh* BCS Fe xxv channel, typically shows the Neupert effect. Low-temperature plasma, which dominates the radiation seen by the *Yohkoh* SXT, rarely shows this property. One cannot use this last fact to argue that the soft X-ray emission is not due to heating by energetic electrons, however. The low-temperature plasma energy may be increasing later in the flare simply because high-temperature plasma is cooling and becoming low-temperature plasma itself. When we look at the total energy in the SXR plasma, we find that approximately one-half (14 of 33) of the flares exhibit the Neupert effect. For the other 19 flares, an additional heating mechanism is indicated.

These results are similar to those reported by Dennis & Zarro (1993), who compared the position of the peaks of the soft X-ray derivative to the peaks of the hard X-ray light curve to determine whether flares were consistent with the Neupert effect. Our method is different, but the results are similar. Dennis & Zarro found that 80% of the flares in their sample showed the Neupert effect. They used the

GOES soft X-ray detector in their study; the *GOES* detector is more sensitive to high-T plasma than the SXT, so one would expect a good level of consistency with the Neupert effect.

It is important to note that the determination of the energy in the different temperature ranges is the result of a rather simple calculation. A more accurate calculation, involving the calculation of the spatially resolved DEM, is clearly necessary. Some ideas of the spatially resolved DEM can be gleaned from close examination of SXT images, by comparison of different filter ratios, and this will be done in future work. The HESSI mission will give imaging and spectroscopic observations of flares for energies down to 3 keV. This will give us images of the high-T plasma continuum emission and the Fe line complex and can be used for DEM calculations in conjunction with *Yohkoh*, SXI, or possibly Solar-B data.

6. CONCLUSIONS

The main conclusions that should be drawn from this work are the following:

1. The solar flare soft X-ray plasma is not isothermal. DEMs for solar flares can be obtained using SXT and BCS data.

2. In the temperature range to which the SXT and BCS are sensitive, the DEM typically decreases with increasing T; some flares show humps in the high-T DEM, but these are smaller than the low-T DEM. This is not what we expect from loop models, for which the DEM increases with T, or decreases gradually, before increasing to a high-T cusp.

3. Even though the DEM is smaller for high T, there can be a substantial amount of energy in the high-T plasma. It should be noted, however, that not all of the energy initially goes into the high-T component, since the low-T component is nonzero at the start of the flare.

4. Higher temperature plasma peaks earlier and cools faster, as is shown for the flares in the sample in Table 1. This is a characteristic of conductive cooling.

5. The Neupert effect is noticeable at high T for almost all of the flares. Roughly one-half of the flares shows this effect when considering the total energy, under the assumption that the total volume occupied by the soft X-ray–emitting plasma remains constant during the flare. Low-T plasma is rarely consistent with the Neupert effect.

REFERENCES

Antiochos, S. K., & Krall, K. R. 1979, ApJ, 229, 788
Antiochos, S. K., & Sturrock, P. A. 1976, Solar Phys., 49, 359
———. 1978, ApJ, 220, 1137
Antonucci, E., & Martin, R. 1995, ApJ, 451, 402
Cargill, P. J., Mariska, J. T., & Antiochos, S. K. 1995, ApJ, 439 1034
Culhane, J. L., et al. 1991, Solar Phys., 136, 89
Cully, S. L., et al. 1997, ApJ, 491, 910
Del Zanna, G., et al. 1996, in ASP Conf. Ser. 109, Cool Stars, Stellar Systems, and the Sun: Ninth Cambridge Workshop, ed. R. Pallavicini & A. K. Dupree (San Francisco: ASP), 259
Dennis, B. R., & Zarro, D. M. 1993, Solar Phys., 146, 177
Dere, K. P., & Cook, J. W. 1979, ApJ, 229, 772
Emslie, A. G. 1985, Solar Phys., 98, 281
Emslie, A. G., Li, P., & Mariska, J. T. 1992, ApJ, 399, 714
Feldman, U., et al. 1996, ApJ, 460, 1034
Fisher, G. H., Canfield, R. C., & McClymont, A. N. 1985a, ApJ, 289, 414
———. 1985b, ApJ, 289, 425
———. 1985c, ApJ, 289, 434
Fisher, G. H., & Hawley, S. L. 1990, ApJ, 357, 243
Fludra, A., & Sylwester, J. 1986, Solar Phys., 105, 323
Gabriel, A. H., et al. 1984, Adv. Space Res., 4 (7), 221
Hudson, H. S., et al. 1994, ApJ, 422, L25
Jakimiec, J., et al. 1984, Adv. Space Res., 4 (7), 23
———. 1992, A&A, 253, 269
Li, P., Emslie, A. G., & Mariska, J. T. 1993, ApJ, 417, 411
Li, P., McTiernan, J. M., & Emslie, A. G. 1997, ApJ, 491, 395
Mariska, J. T., Emslie, A. G., & Li, P. 1989, ApJ, 341, 1067

Masuda, S., et al. 1994, Nature, 371, 495
McTiernan, J. M. 1996, in Magnetic Reconnection in the Solar Atmosphere: Proceedings of a *Yohkoh* Conference, ed. R. D. Bentley & J. T. Mariska (San Francisco: ASP), 228
McTiernan, J. M., et al. 1993, ApJ, 416, L91
Metcalf, T. R., et al. 1996, ApJ, 466, 585
Mewe, R., et al. 1996, in in ASP Conf. Ser. 109, Cool Stars, Stellar Systems, and the Sun: Ninth Cambridge Workshop, ed. R. Pallavicini & A. K. Dupree (San Francisco: ASP), 273
———. 1997, A&A, 320, 147
Meyer, J. P. 1985, ApJS, 57, 173
Monsignori-Fossi, B. C., et al. 1996, ApJ, 466, 427
Nagai, F., & Emslie, A. G. 1984, ApJ, 279, 896
Neupert, W. M. 1968, ApJ, 153, L59
Newton, E. K., Emslie A. G., & Mariska J. T. 1995, ApJ, 447, 915
———. 1996, ApJ, 459, 804
Press, W. M., et al. 1986, Numerical Recipes (New York: Cambridge Univ. Press), chap. 10
Reale, F., et al. 1997, A&A, 325, 782
Sakao, T. 1994, Ph.D. thesis, Univ. Tokyo
Serio, S., et al. 1991, A&A, 241, 197
Strong, K. T., et al. 1986, in NASA Conf. Pub. 2439, Energetic Phenomena on the Sun, The Solar Maximum Mission Flare Workshop Proceedings, ed. M. Kundu & B. Woodgate (Washington, DC: NASA), § 5.3
Sylwester, B., et al 1993, A&A, 267, 586
Sylwester, J., Schrijver, J., & Mewe, R. 1980, Solar Phys., 67, 285
Tsuneta, S., et al. 1991, Solar Phys., 136, 37